SUPPORT VECTOR MACHINE MODELS FOR DIABETIC RETINOPATHY DIAGNOSIS AND GRADING

Jigme Namgyal and Eckart Schulz*

Received: July 31, 2022; Revised: September 09, 2022; Accepted: November 07, 2022

Abstract

This work applies five variants of the support vector machine to the classification of the various stages of nonproliferative diabetic retinopathy. Four hundred eye fundus images from the Messidor repository are preprocessed and thirteen features extracted. The features best suited as inputs for support vector machine classification are identified. Initially, binary classification of severe nonproliferative diabetic retinopathy alone versus a normal eye is performed, achieving an accuracy of 97.44% using the standard support vector machine with Gaussian kernel and when optimized for accuracy. When optimized for sensitivity, the twin bounded support vector machine achieves the highest sensitivity of 99.06%. Then multiclass grading into all four stages of nonproliferative diabetic retinopathy is performed. Best performance with regards to four performance metrics, namely accuracy, sensitivity, specificity, and precision is achieved with the twin bounded support vector machine variant, when one-versus-one decision configuration is used in combination with a novel decision strategy that includes accumulated distances from the decision hyperplanes in the decision algorithm. The results compare favorably with data published in the literature.

Keywords: Decision strategy; Diabetic retinopathy; Multiclass decision; Support vector machine

Introduction

The eye is a very delicate organ, yet of great importance in a person's daily life. With increasingly sedentary lifestyles and longevity being observed, the share of the population that suffers from health issues affecting the eye such as high blood pressure or diabetes, has risen worldwide to previously unknown levels. The World Health Organization (2015) reported that around 422 million people in the world suffer from Diabetes Mellitus, a figure that is expected to rocket to an even higher number in the years to come.

One of the most common complications in people living with diabetes is a condition called diabetic retinopathy (DR). Affecting 25-44% of the diabetes patients at some point in their life (American Academy of Ophthalmology, 2019), it is caused by increased glucose levels that damage the blood vessels of the retina, making it become leaky or blocked. In the advanced stage of the disease, abnormal blood vessels appear from the retina which can bleed and cause retinal scarring and lead to permanent vision loss or blindness. It is thus important to detect early signs of diabetic retinopathy in a patient, in order to take measures which can delay or mitigate the deterioration of the eye.

School of Mathematics, Suranaree University of Technology, Nakhon Ratchasima 30000, Thailand.
*E-mail: jigmenamgyal.cst@rub.edu.bt; eckart@g.sut.ac.th**
* *Corresponding Author*
DOI:

Suranaree J. Sci. Technol. 30(3):030109(1-16)

Clinically visible features associated with DR are the presence of microaneurysms, haemorrhages, hard and soft exudates, intraretinal microvascular abnormalities (IRMA), venous beading and neovascularization. Broadly, DR can be classified into proliferative type (PDR) and three stages of nonproliferative (NPDR) type as follows:

1. *Mild nonproliferative DR.* A few microaneurysms can be observed with no noticeable effect on vision and no other significant findings.
2. *Moderate nonproliferative DR.* The presence of several microaneurysms, a tiny amount of haemorrhages, and cotton-wool spots characterizes this condition. There may also be a mild degree of venous beading and IRMA.
3. *Severe nonproliferative DR.* This is characterized by a large number of severe microaneurysms, haemorrhages, cotton-wool spots, venous beading and IRMA.
4. *Proliferative DR.* This is an advanced stage of DR. In addition to the findings from the NPDR, other findings such as retinal neovascularization and vitreous haemorrhages can be seen. Severe visual loss will be noticed by the patients.

In this work, only the different stages of NPDR are considered, as patients with PDR are already noticeably visually impaired and detection is thus no longer required.

Machine-Aided Retinopathy Detection

The rapid progress in computing technology achieved in recent years has made possible the development of a great variety of computing tools to assist physicians in diagnosis and treatment. An important component of diagnosis is to decide whether a patient suffers from some particular ailment and to determine to what degree.

The machine-aided detection of diseases of the eye is an ongoing and very active field of research. The techniques consist of two essential steps: Image preprocessing, to identify, highlight and extract the relevant features from an image, followed by model selection and training. Neural networks and support vector machines are popular tools employed for this latter task.

Acharya *et al*. (2008) proposed an automated grading of diabetic retinopathy stages by a multiclass directed acyclic graph support vector machine algorithm. A total of 300 retinal fundus images with 60 subjects each from normal, mild, moderate, and severe nonproliferative diabetic retinopathy, as well as proliferative diabetic retinopathy were used. Histogram equalization was applied as a preprocessing technique. The preprocessed grayscale images were then converted to one-dimensional data using a Radon transform. Then 18 features were extracted using higher order spectra from which four features were selected using the statistical p-test. On classification, an accuracy and sensitivity of 82% and a specificity of 88% were obtained.

Because the growth of new blood vessels is a typical sign of advanced diabetic retinopathy, the authors of (Welikala *et al*., 2015) focus on the detection of new abnormal blood vessels. They use two support vector machines, one to distinguish new blood vessels from normal blood vessels, and a second one to distinguish new blood vessels from exudates. A genetic algorithm is used for feature selection. Image regions are identified as new blood vessels only when both machines agree.

Imani *et al*. (2015) use the variance of shearlet coefficients to first identify whether the blood vessels in an image are of sufficient quality for automatic processing. This is followed by morphological component analysis using shearlet and curvelet transform to separate out retinal vessels and exudates. Then they extract local features and compare them to a database of these features that has been created from a pool of training images, achieving an accuracy of 92.82% for binary classification.

Carrera *et al*. (2017) proposed computer assisted diagnosis of severe non-proliferative diabetic retinopathy and classification of its various stages by support vector machines. In total 400 optic fundus images were considered. For feature extraction, blood vessels were segmented, and their densities obtained, microaneurysms and hard exudates were isolated. Eight features were extracted and fed to the support vector machine classifier. Sensitivity of 94.6% and overall predictive capacity of up to 94% were reported for severe NPDR recognition.

James *et al*. (2018) introduced a method to detect exudates by morphological operations, blood vessels and haemorrhages by complement function, and microaneurysms by edge detection techniques. Relevant features were obtained and a multilayered feed forward neural network was used for classification.

Two deep convolutional neural networks to construct features from an image were employed by Li *et al*. (2019). Combined with other features extracted directly from the image, they trained a multiclass support vector machine for severity grading, including nonproliferative and proliferative diabetic retinopathy and report an accuracy of 86.17%.

A comprehensive review of recent publications on diabetic eye and other eye disease detection through deep learning was given by Sarki *et al*. (2020). Practically all publications reviewed make use of convolutional neural networks. Of the referenced papers, Ghosh *et al*. (2017) obtain an accuracy of about 95% for binary classification, and of 85% for multiclass detection on a dataset which includes proliferative diabetic retinopthy, whereas Hemanth *et al*. (2020) obtain binary classification accuracy of 97%.

Kandhasamy *et al*. (2017) have presented a multi level set segmentation algorithm and support vector machine with selective features along with genetic algorithm for diabetic retinopathy severity grading. Mathematical morphological operations and principal component analysis were used for clustering before the feature extraction. They reported areas under receiver operating curve of 98.01% on average for all severity levels.

A hierarchical severity grading system for detection and classification of nonproliferative diabetic retinopathy was studied by Bhardwaj *et al*. (2020), who employed support vector machine and k-nearest neighbor classifiers. From statistical analysis, 12 optimal features were obtained and fed to the respective classifiers. It was concluded that the k-nearest neighbor classifier achieved best accuracy and computation time both in classifying diabetic and non-diabetic retinopathy images and in grading the severity levels of diabetic retinopathy cases.

An interracial DR screening artificial intelligence (AI) created model was developed by Katada *et al*. (2020). Convolutional neural network and support vector machine were used to train the model on an American fundus dataset. They showed that the trained AI model exhibited even higher sensitivity and specificity when tested on another 200 Japanese subjects.

Dandapat *et al*. (2021) compare support vector machine, k-nearest neighbor and convolutional neural networks for binary diabetic retinopathy detection and obtain accuracies of 96.62%, 94.38% and 94.74%, respectively.

Overall, most publications using support vector machine focus on binary classification and use the standard support vector machine. There are only few reports on the multiclass detection of diabetic retinopathy by support vector machines. It should be noted that the results published in the literature are not directly comparable as they may be using different datasets.

Support Vector Machines

A common tool for decision making in machine learning is the Support Vector Machine (SVM). The papers by Carrera *et al*. (2017) and Kandhasamy *et al*. (2017) show that support vector machines can be employed for diabetic retinopathy classification with success.

Numerous variants of the support vector machine model have been introduced in recent years, with the goal to improve training speed and decision performance. The most common of these are the Least Squares SVM and the Twin SVM. These have undergone further modifications to obtain, for example, the Twin Bounded SVM, the Least Squares Twin SVM and the Improved Least Squares Twin SVM. In addition, when it comes to multiclass decisions, as is the case in the grading of nonproliferative diabetic retinopathy, several decision strategies are availabe, including the one-versus-one (OVO), one-versus-all (OVA) and the all-versus-one (AVO) strategies.

Since support vector machines are known to be good classifiers, this work, therefore, aims at evaluating the above support vector machine variants and decision strategies with regards to performance in nonproliferative retinopathy detection and classification. It is assumed that the reader is familiar with the above listed SVM models and decision strategies; surveys can be found in the papers by Ali *et al*. (2021) or Namgyal and Schulz (2022).

Materials and Methods

This work used the Messidor database (Decencière *et al*., 2014), first ophthalmologic department, which consists of 400 eye fundus colour images and is freely available. The images were captured using 8 bits per colour plane at 2240×1488 pixels. All images are in TIFF format, and an Excel file with medical diagnoses by experts is also provided, who have graded the images based on the severity level of the disease; grade 0 for normal, grade 1 for mild NPDR, grade 2 for moderate NPDR, and grade 3 for severe NPDR. The database contains 152 normal, 30 mild, 69 moderate and 149 severe NPDR fundus eye images.

The research procedure consists of two main steps: Image preprocessing, and image classification. A general flowchart is presented in Figure 1.

1. *Image preprocessing.* The retinal eye fundus images were first processed to enhance and detect eye abnormalities and to extract the features best suited as data input for classification.
2. *Image classification*. Two types of classification were performed. In binary

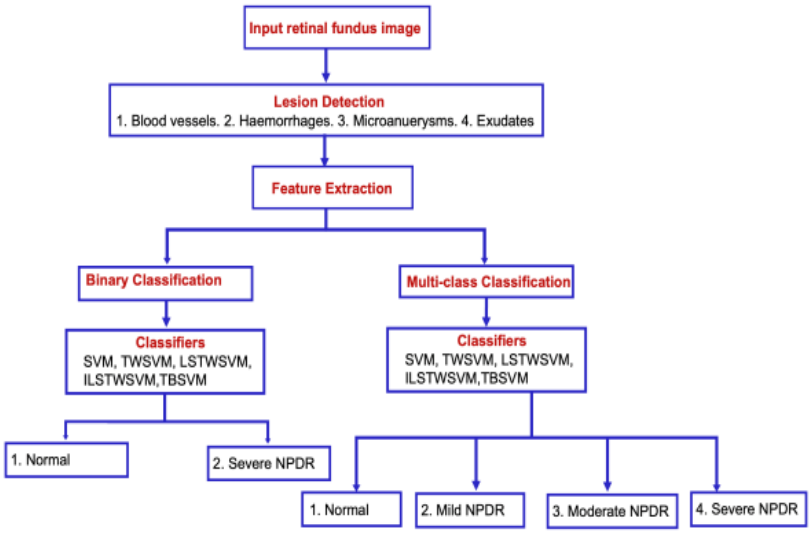

Figure 1. Flowchart of the proposed methodology

classification, the SVM models were evaluated for distinguishing between images with severe NDPR and healthy images. In multi-class classification, the models were evaluated for performance in the classification of the various stages of NPDR in the images.

Image Preprocessing

To enhance the image and for the better segmentation outcomes, the fundus images were processed using techniques such as described in (Gonzalez *et al*., 2009). Because the classification results depend on the outcome of this preprocessing step to a large degree, we provide a detailed description in the following.

First the images were cropped to 738×727 pixels to get the proper field of view and reduce computational costs. The images in RGB colour format had a certain degree of variation in the colour. To have some sort of uniform threshold level during the segmentation processes, all images were colour normalized using one of the high quality images as a reference image as defined in equation (1) below. Then the images were examined for sharpness level. Blurry images were sharpened accordingly, since the objects of interest could not be seen clearly, let alone detected. Then each colour band was extracted, namely, the red, green, and blue channels, and compared. The green channel image provided the highest contrast on the objects of interest from the background, whereas the red and blue channel images showed poor contrast as well as noise. For all the different segmentation processes, we therefore used the green channel image, with the exception of the optic disc detection, where we considered the red band.

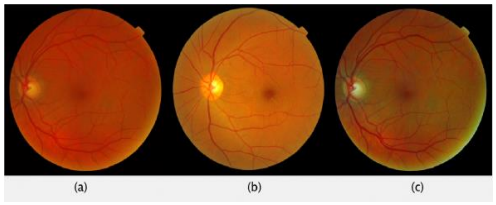

Figure 2. Image colour normalization. (a) Input image. (b) Reference image. (c) Colour normalized

Colour Normalization

Let *f(x,y)* be any of the red, green and blue channels of an image and *h(x,y)* those of a reference image, all converted to type double from uint8 for numerical computation. Then, as per Chen *et al.* (2020), the colour normalization of image *f* using *h* as a reference is defined by the equation:

$$f_{\text{cn}} = \frac{\sigma_R}{\sigma}(f - \mu) + \mu_R \qquad (1)$$

where μ and μ_R are the mean intensities and σ and σ_R the standard deviations of the channel f and h respectively, and $f_{\text{cn}}$is the corresponding channel of the new colour normalized image. The image composed of the three new channels f_{cn} is said to have similar colour distribution as the reference image *h*. Figure 2 illustrates this process.

Lesion Detection

Retinal blood vessels segmentation. In the detection of diabetic retinopathy from eye fundus photographs, the identification of blood vessels is an important step. There are certain abnormalities that those vessels can present in an affected eye. For instance, if the disease has already advanced to a

later stage, then a change in the shape of those vessels and some abnormal new growth can be observed.

In segmenting the retinal vessels, we closely followed the work by Ramos-Soto *et al*. (2021), who introduced optimized top-hat transformation and applied homomorphic filtering. However, for thresholding we used Otsu's thresholding technique throughout.

The extracted green channel image was first filtered using a Gaussian filter with standard deviation of σ = 0.68. This operation enhances the image structures and suppresses the noise generated from image sharpening.

We focus on the segmentation of thick and thin vessels separately and merge them at the end.

Thick vessels extraction. Represent an image of $M \times N$ pixels as an $M \times N$ matrix $I = [f_{ij}]$ with integer pixel values, $0 \leq f_{ij} \leq 255$. Firstly, the Gaussian filtered image I was inverted, denoted I^C, and defined as

$$I^C = U - I$$

where U is the $M \times N$ matrix all of whose entries are the maximum pixel values of 255.

We define two disk shaped structuring elements, namely S_1 and S_2, of radii 8 and 16 pixels respectively. Then the morphological opening of I^C by S_1 was performed, that is,

$$I_{\text{op}} = I^C \circ S_1, \quad (2)$$

followed by a closing operation on (2)

$$I_{\text{cl}} = I_{\text{op}} \bullet S_2. \quad (3)$$

Then the Figure 3 was subtracted from I^C, resulting in an enhanced image. This process is called an optimized top-hat transformation.

Next, a homomorphic filter was applied on the resultant image to further enhance the thick vessels. Homomorphic filtering is a filtering technique in the frequency domain which enables adjustments on illumination and reflectance components of an image. The resulting image was then filtered by a median filter to remove salt and pepper noise. Once again, the filtered image underwent another optimized top-hat transformation with disk shaped structuring elements of radii 32 and 64 pixels. This fills small holes in the vessels and enhances the structures. Finally, the image was binarized using Otsu's thresholding method, where the algorithm chooses the threshold automatically. Because haemorrhages and blood vessels have similar intensity values, the haemorrhages were also detected together with the blood vessels. To overcome this, we removed components whose total number of pixels were less than 300. The final image now represents the extracted thick vessels. The whole procedure is depicted in Figure 3.

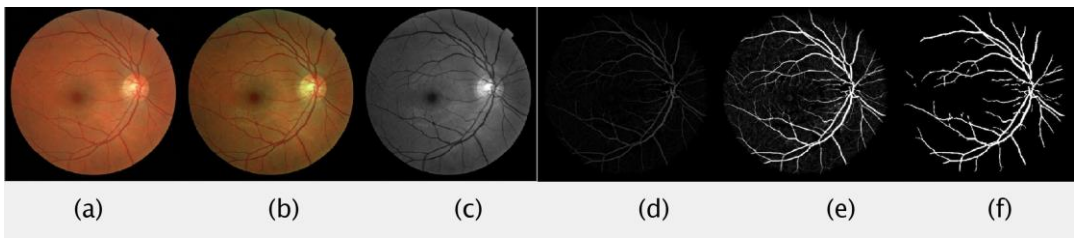

Figure 3. Thick vessels extraction. (a) Original image. (b) Colour normalized. (c) Green channel image. (d) Optimized top-hat transformed image. (e) Homomorphic filtered and (f) Thick vessels extracted by thresholding

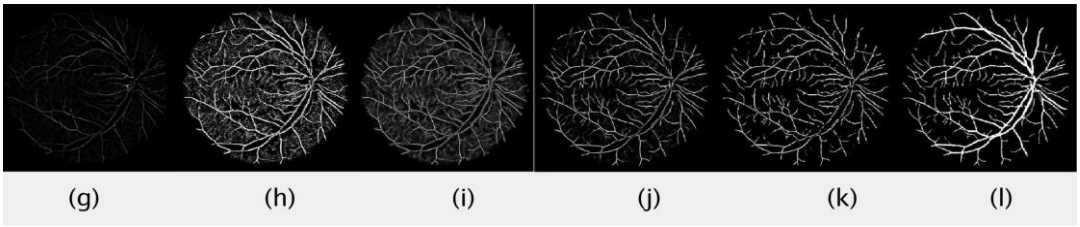

Figure 4. Thin vessels extraction and final segmentation. (g) Optimized top-hat for thin vessels. (h) Homomorphic filtered. (i) 2-D match filtered. (j) Contrast adjusted before thresholding. (k) Thin vessels after binarization. (l) Blood vessels segmented after adding images (f) and (k), and noise reduced

Thin vessels extraction. For this procedure, as shown in Figure 4, we also used the optimized top-hat transformation, but the radii of S_1 and S_2 were taken as 4 and 20 pixels respectively. This is due to the thin vessels spanning over smaller structural regions. Then a homomorphic filter was applied followed by two-dimensional matched filtering. The concept of two-dimensional matched filtering is that it can enhance certain regions of an image that matches some estimated distribution curve of the image. So, the method finds whether the distribution is correlated to the local image area.

Microaneurysms detection. Microaneurysms are among the most important clinical pathologies in the identification of diabetic retinopathy. These are swollen tiny vessels, and are the first abnormalities that develop. They are visible as tiny blobs at the end of capillaries. If this is detected early on, patients can delay the progression of the disease with treatment, ultimately saving their eyesight.

First we took the complement I^C of the green channel image. Then this complement I^C was corrected for the non-uniform background using a morphological open-close filtering technique called alternate sequential filtering (Gonzalez *et al.*, 2009). This method uses a combination of morphological openings and closings with a series of structuring elements. We chose flat disk-shaped structuring elements S_i, $i = 1,2,..,12$, with radii $r_i = 2,3,...,13$, and performed open-close filtering, that is,

$$I_{\text{ocf}} = (I^C \circ S_i) \bullet S_i, \quad i = 1,2,\dots,12. \tag{4}$$

The resultant image I_{ocf} yielded a smooth and uniform background. Then the background image I_{ocf} was subtracted from I^C,

$$I_{\text{enh}} = I^C - I_{\text{ocf}} \tag{5}$$

to obtain the now image background corrected enhanced image I_{enh}. Next, contrast adjustment was made to this image to highlight the tiny regions corresponding to the microaneurysms. Then this image was morphologically reconstructed using the marker image

$$I_{\text{mark}} = I_{\text{enh}} \otimes I_{\text{bv}},$$

where I_{enh} is the contrast adjusted image, I_{bv} is the blood vessels mask from Figure 4, and $\otimes$ denotes element-wise matrix multiplication. The reconstructed image

$$I_{\text{rc}} = R_{I_{\text{mark}}}(I_{\text{enh}}),$$

was subtracted from the contrasted adjusted image I_{enh} and binarized, denoted I_{bw}, setting a threshold of $t = 53\%$ of the maximum intensity obtained by trial and error. The binarized image contains the tiny components arising from the microaneurysms, other remnants left behind by the blood vessels and haemorrhages, background artefacts and some noise. We filtered the image I_{bw} further using connected component analysis. Each connected component in the image was labelled. Then we filtered for microaneurysms using the following set of features in the analysis:

1. *Area*. Total number of white pixels in each connected component.
2. *Major axis length*. Length of the major axis of the ellipse approximating the connected component. (To be precise, this is the ellipse which has the same normalized second central moment as the region.)
3. *Minor axis length*. Length of the minor axis of the ellipse approximating the connected component.
4. *Circularity*. This is a measure of roundness of an object defined by

$$\text{circularity} = \frac{4\pi \cdot \text{Area}}{P^2},$$

where P denotes the perimeter which is computed as the sum of boundary pixels of an object.

5. *Eccentricity*. This is defined as the ratio of distance between foci of the ellipse to its major axis length.

Using the features mentioned above, we set area $\in$[5, 22] pixels, circularity $\in$ [1, 2.5], eccentricity ≤ 0.9, and the ratio of major axis length to minor axis length should be in the range [1,2.5] for microaneurysms. This leads to removal of noise and objects which are not microaneurysms. The final image contains the detected microaneurysms. The whole process is illustrated in Figure 5.

Haemorrhages detection. Haemorrhages in the fundus eye images have similar intensity levels to blood vessels and microaneurysms. Due to this, the haemorrhage segmentation method is akin to the microaneurysm identification process.

First, the inverted green component image was background corrected. Then the image was filtered with a median filter to suppress noise, followed by contrast adjustment. Next, the homomorphic filter was applied which further enhanced the structure of haemorrhages. The image was then binarized, denoted I_{bwh}. Since I_{bwh} also contains blood vessels, we subtracted the detected blood vessels, that is,

$$I_{\text{hm}} = I_{\text{bwh}} - I_{\text{bv}} \tag{6}$$

where I_{bw} is the retinal blood vessels mask obtained in Figure 4.

The image I_{hm} still contained false positive foreground pixels from the background and noise. For this, we performed mean intensity pixel analysis by labelling all the connected components.

1. For each connected component, compute its mean intensity value in the green channel.
2. Remove the blobs or regions whose mean intensity in the green channel is greater than 95.

Furthermore, some blood vessels could still be observed in the image. To overcome this, we once again performed the connected component analysis based on eccentricity. Those components whose eccentricity did not lie within [0, 0.097] were disposed of. In addition, the connected components with area less than 25 pixels were discarded since they overlap with microaneurysms. The final filtered image contains the retinal haemorrhages as shown in Figure 6.

Exudates detection. In contrast to blood vessels, haemorrhages and microaneurysms, exudates have higher intensity values since they are yellowish bright fluffy patches seen in the diseased retinal imaes. Due to this, colour normalization is not advised as it would reduce the intensity values of exudates, counter-acting the goal of their extraction. An overview of the exudate's segmentation process is outlined in Figure 7.

In this procedure, we work with the green channel image itself instead of inverting it.

Background correction is also necessary. For this we used the morphological close-open filtering technique

$$I_{cof} = (I_{gch} \bullet S_1) \circ S_2 \quad (7)$$

where I_{gch} is the green channel image and S_1 and S_2 are disk shaped structuring elements with radii of 25 and 30 pixels respectively. Then the background corrected image is

$$I_{enhe} = I_{gch} - I_{cof}. \quad (8)$$

The image I_{enhe} revealed a high level of contrast between the exudates and background while other features were significantly suppressed as desired.

Further structure enhancement was made on the Figure 8, by application of a homomorphic filter. The resulting image is denoted by I_{hf}.

On I_{hf} we suppressed objects with pixel values below 50 since exudates usually exhibit higher intensity levels. To denoise the image and remove background artefacts, we labelled the connected components and examined their mean intensities in the green plane. The regions with mean intensity value below 51 were removed. In addition, the connected components of area below 5 pixels were discarded since they usually represent noise.

The optic disc region was still visible in the binarized image because its intensity values are similar to exudates. Thus, the optic disc was removed using the mask generated by optic disc segmentation as explained below and shown in Figure 8.

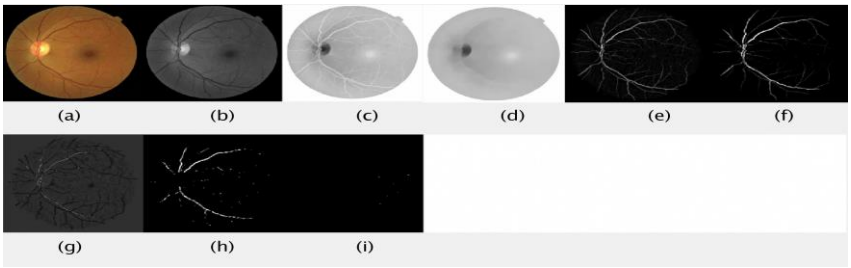

Figure 5. Microaneurysms detection. (a) Original image. (b) Green component. (c) Complement of (b). (d) Background estimation. (e) Subtraction of (d) from (c). (f) Contrast adjusted. (g) Morphologically reconstructed image. (h) Binarized image, and (i) After connected component analysis

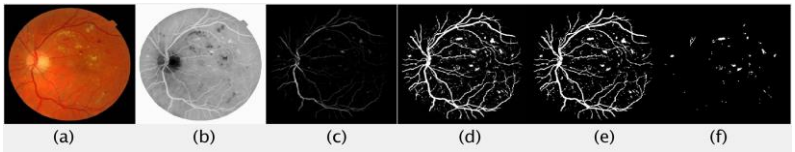

Figure 6. Haemorrhages detection. (a) Original colour normalized image. (b) Inverted green channel image. (c) Background corrected. (d) Homomorphic filtered. (e) Thresholded image, and (f) Blood vessels subtraction and connected component analyzed leading to haemorrhages segmentation

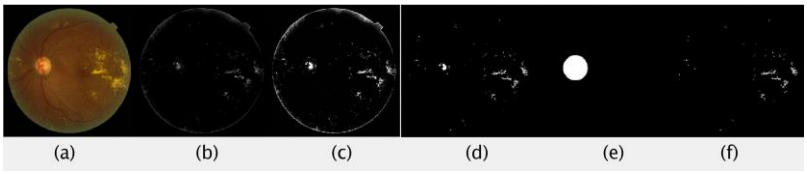

Figure 7. Exudates detection. (a) Original image. (b) Exudates highlighted on green component after background illumination correction by close-open filtering. (c) Lower intensity pixel values suppressed. (d) Binary image containing exudates and optic disk. (e) optic disk mask. (f) Exudates detected after removing OD region by OD mask in (e)

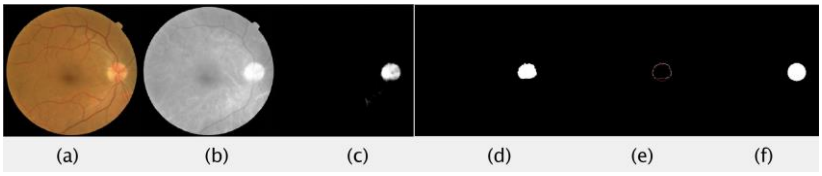

Figure 8. Optic disk segmentation. (a) Original image. (b) Red channel image. (c) Background suppressed (b) After colour normalization. (d) Binarized and morphologically closed image. (e) Canny edge detection and circular Hough transform, and (f) OD mask

Optic disc segmentation. The optic disk is seen as a bright circular shaped object and it is an entrance to the major blood vessels supplied to the retina. It displays one of the highest intensity values besides exudates in the retinal fundus photographs.

For optic disk detection we first colour normalized the input image as in equation (1), however, we decreased the mean value μ of the image f by the value of 0.5. This had the outcome of significantly suppressing regions with intensity values less than that of the optic disk.

Then we extracted the red channel from the colour normalized image since this channel possesses higher contrast around the optic disk region. The extracted image was then binarized and morphologically closed to maintain connectedness. The binarized image was further filtered labelling connected components. Each component was then examined for the total area and circularity. The conditions set are: area $\in$ [3500, 15000] pixels, and the circularity ≥ 0.7. Then the Canny edge detection method was employed to get the round edge of the remaining components. Finally, a circular Hough transform was applied with radius specification given in the range of 45 to 65 pixels. This transformation detected a disk-shaped region, which was the optic disk to be segmented.

Feature extraction

From the detected lesions, we extracted the following set of features to be used as input vectors for the classification of DR:

1. Area of retinal blood vessels, which is the sum of non-zero pixels in a segmented image from blood vessels.
2. Area of haemorrhages.
3. Number of microaneurysms.
4. Area of microaneurysms.
5. Area of exudates.

Furthermore, based on the green channel image, we used the following statistical texture features and gray-level co-occurrence matrix (GLCM) features:

6. Average intensity of the image.
7. Average contrast of the image.
8. Smoothness.
9. Third moment.
10. Energy.
11. Entropy.
12. Homogeneity.
13. Maximum probability.
14. Entropy from GLCM.

Results and Discussion

We present the results from different classification models, namely, the standard support vector machine (SVM), the twin SVM (TWSVM), twin bounded SVM (TBSVM), least squares twin SVM (LSTSVM), and improved least squares twin SVM (ILSTSVM), on detection of NPDR. For a detailed description of these models and the various decision strategies employed in the multiclass case (one-versus-one (OVO), one-versus-all (OVA), all-versus-one (AVO), maximum vote (mv), mean average distance (md) and mean average distance as a tie breaker (mv+md) we refer to (Namgyal and Schulz, 2022).

All computations were done using MATLAB Version 9.7 (R2019b). The image segmentation

processes were performed with the help of the image processing toolbox, and the binary and multi-class DR classifications with the statistics and machine learning toolbox and libsvm (Chang and Lin, 2017). Where available, twin SVM packages were used. We used a personal Macbook CPU version i5 1.8GHz Dual-Core, memory 8 GB, system MacOS 64 bit.

Model selection and validation. For all support vector machine models, the Gaussian (RBF) kernel was employed as it showed superior performance over the linear or the polynomial kernels. It is of the form

$$K(\vec{x},\vec{y}) = exp\left(-\frac{||\vec{x}-\vec{y}||^2}{2\sigma^2}\right)$$

where σ is the kernel parameter.

Standard performance metrics were used for binary (positive vs. negative) classification, all expressed in percentages:

$$\text{Accuracy} = \frac{\text{TP+TN}}{\text{TP+TN+FP+FN}}$$
$$\text{Sensitivity} = \frac{\text{TP}}{\text{TP+FN}}$$
$$\text{Specificity} = \frac{\text{TN}}{\text{TN+FP}}$$
$$\text{Precision} = \frac{\text{TP}}{\text{TP+FP}}$$

where TP (TN) denotes the number of samples correctly identified as positive (resp. negative), and FP (FN) the number of samples incorrectly identified as positive (resp. negative).

To evaluate the performance of the machine learning models and to overcome the problem of over-fitting, *k*-fold cross validation was used. All results listed in the tables show averages over ten runs of 10-fold validation together with the standard deviations.

Parameter selection. SVM classifiers are heavily influenced by the a-priori chosen parameters. Therefore, we optimized the model parameters for better performance using the grid search technique. In the standard SVM there are two parameters, viz. the penalty parameter C and kernel parameter σ. However, for the TWSVM and LSTSVM there are now two penalty parameters C_1, C_2, while the TBSVM and ILSTSVM have four penalty parameters C_1, C_2, C_3, C_4. To reduce computational complexity in parameter optimization, we set C_1=C_2 and C_3=C_4. The penalty parameters were selected from the set $\{2^i : i = -20, ...,15\}$ and the kernel parameter σ from the set $\{2^i : i = -10,...,10\}$.

Binary Classification of Severe NPDR

All 152 normal images and 149 severe NPDR images contained in the Messidor database were used for binary classification.

Feature selection. Besides optimizing the parameter values, we also optimized for the number and type of input features by experiment.

In the case of binary classification we identified 7 from the total of 13 extracted features as giving optimal results to be used. These are the the number and area of microaneurysms, the area of haemorrhages, the area of exudates, entropy, the third moment of the green channel image, and finally the measure of randomness computed from the gray-level co-occurrence matrix (GLCM). Parameter optimization was performed with respect to two metrics: accuracy and sensitivity.

Accuracy optimization. The classification results from parameter selection optimized for accuracy are shown in Table 1. The highest accuracy of 97.44±2.91% was achieved by the standard SVM model. As for specificity and precision, however, the TBSVM obtained the highest rates: 98.68±3.12% and 98.71±2.99%, respectively. Of all the models tested, the LSTSVM achieved the lowest performance.

Sensitivity optimization. In medical diagnosis it is most important to catch as many of those infected as possible. A false positive result is thus more acceptable than a false negative result. That is, instead of accuracy one needs to maximize the ratio

$$\frac{\text{number of positive results among the infected}}{\text{total number of infected}}$$

which is sensitivity.

In the case at hand, this means that the machine learning models should not misclassify eye fundus photographs that show signs of disease as healthy

Table 1. Accuracy optimized binary classification for NPDR detection

	SVM (C, σ)	**TWSVM (C_1=C_2, σ)**	**TBSVM (C_1=C_2, C_3=C_4 σ)**	**LSTSVM (C_1=C_2, σ)**	**ILSTSVM (C_1=C_2, C_3=C_4 σ)**
Parameters	2^{12}, 2^0	2^1, 2^{-1}	$2^{0.75}$, 2^{-8}, 2^{-2}	2^{-6}, 2^0	2^{-6}, $2^{-12.25}$, 2^{-1}
Accuracy	97.44 ± 2.91	96.44 ± 3.41	96.87 ± 2.71	95.25 ± 4.14	96.11 ± 3.42
Sensitivity	96.65 ± 4.52	95.31 ± 5.86	95.04 ± 4.57	92.69 ± 7.76	95.78 ± 6.06
Specificity	98.22 ± 3.75	97.57 ± 4.46	98.68 ± 3.12	97.75 ± 4.03	97.00 ± 4.81
Precision	98.3 ± 3.48	97.65 ± 4.19	98.71 ± 2.99	97.79 ± 3.85	97.13 ± 4.41

Table 2. Sensitivity optimized binary classification for NPDR detection

	SVM (C, σ)	TWSVM (C_1=C_2, σ)	TBSVM (C_1=C_2, C_3=C_4 σ)	LSTSVM (C_1=C_2, σ)	ILSTSVM (C_1=C_2, C_3=C_4 σ)
Parameters	2^{-4}, $2^{9.75}$	2^{-6}, 2^{7}	2^{-6}, $2^{-13.5}$, $2^{7.5}$	$2^{-8.5}$, $2^{1.5}$	$2^{-7.25}$, 2^{-11}, $2^{0.5}$
Accuracy	90.17 ± 4.80	91.86 ± 4.64	91.53 ± 4.77	93.52 ± 4.21	94.05 ± 4.19
Sensitivity	98.35 ± 3.35	98.80 ± 2.74	99.06 ± 2.52	98.60 ± 2.92	98.66 ± 3.01
Specificity	82.55 ± 8.94	85.05 ± 9.02	84.18 ± 9.53	88.53 ± 7.99	89.53 ± 7.40
Precision	85.10 ± 6.89	87.17 ± 6.80	86.56 ± 7.26	89.89 ± 6.52	90.63 ± 6.20

eye images. Thus, we alternatively optimized the parameters for better performance in terms of sensitivity. The results are shown in Table 2. It can be seen that the TBSVM achieved the highest sensitivity of 99.06±2.52%, whereas accuracy, precision and specificity measures have dropped substantially throughout. The smallest drop can be observed with the LSTSVM and ILSTSVM models which now have become the leaders in all categories other than sensitivity, while still showing good sensitivity.

Multiclass Grading of NPDR

Since NPDR has three clinical stages, we performed multi-class classification using the same SVM classifiers as in the binary case. We adopted the classification strategies one-versus-all (OVA) and one-versus-one (OVO) for all models, and in addition, all-versus-one (AVO) for the twin-type SVM models. In addition, we used the minimum average distance strategies (md and mv+md) introduced in (Namgyal and Schulz, 2022) for the twin-type SVMs.

Multiclass metrics. In the multi-class case, one can distinguish between two accuracies: Accuracy-1 measures the fraction of correctly identified samples. If S denotes the total number of samples, S_i the number of samples in class i, S_{ij} the number of samples in class i that are classified to belong to class j, and N the number of classes, then

$$\text{Accuracy-1} = \frac{\sum_i S_{ii}}{S}$$

Accuracy-2 and the remainig metrics are obtained as averages for each individual class. For example, setting

$$\text{Ac}_i = \frac{S_{ii} + \sum_{j\neq i}\sum_{k\neq i} S_{jk}}{S}$$

which is the fraction of samples correctly identified as belonging to class i (corresponding to TP in binary classification), or not belonging to class i (corresponding to TN), then

$$\text{Accuracy-2} = \frac{1}{N}\sum_i \text{Ac}_i$$

Similarly,

$$\text{Sensitivity} = \frac{1}{N}\sum_i \text{Se}_i,\ \text{Se}_i = \frac{S_{ii}}{S_i}$$

$$\text{Specificity} = \frac{1}{N}\sum_i \text{Sp}_i,\ \text{Sp}_i = \frac{\sum_{j\neq i}\sum_{k\neq i} S_{jk}}{\sum_{j\neq i} S_j}$$

$$\text{Precision} = \frac{1}{N}\sum_i \text{Pr}_i,\ Pr_i = \frac{S_{ii}}{\sum_j S_{ji}},$$

all reported in percentages.

Feature selection. In multiclass decision we also searched for the optimal number of features by experiment. We obtained optimal results when supplying 11 of the 13 features to the classifiers: the number of microaneurysms, the areas of microaneurysms, of haemorrhages and of exudates, energy, homogeneity, maximum probability, average intensity, average contrast, smoothness and the third moment of the green channel. Parameters were optimized for best accuracy-1 performance.

Classification Results

The multiclass decisions are shown in Tables 3 and 4.

(i) One-versus-one results

The one-versus-one (OVO) classification results in Table 3 indicate that the TBSVM, after replacing the standard maximum-votes (mv) with the 'maximum-votes and minimum average distance tiebreaker' (mv+md) decision strategy introduced in (Namgyal and Schulz, 2022), shows the highest scores in both, accuracy-1 and accuracy-2 at rates of 75.18±5.52% and 87.59±0.31%, respectively. Other metrics like sensitivity, specificity and precision were also highest for this machine.

Similarly, the TWSVM, after switching to the mv+md strategy, shows a slight performance increase.

Overall the LSTSVM gave the lowest performance rates with an accuracy-1 of 71.35±5.48% and sensitivity of 50.97% ±1.53%. It can be noticed, however, that for the two least squares twin SVM models (LSTSVM and ILSTSVM), classification by the novel minimum average distance (md) gave noticeably better performance than the standard maximum-votes (mv) strategy.

This is illustrated with the sample confusion matrices for the TBSVM (mv+md) and the LSTSVM in Figure 9. They show that the TBSVM performs fairly better in classifying normal and severe NPDR images than the LSTSVM. Yet, most of the images in the mild class and nearly half of the images in the moderate class are being misclassified as normal with the TBSVM. The situation further deteriorates in the LSTSVM as even 17 of the 149 severe images are classified as normal, in addition to the misclassified mild and moderate images.

(ii) One-versus-all and all-versus-one results

In OVA and AVO classifications, the usual SVM, the TWSVM and TBSVM show similar performance, with the TBSVM edging out a small lead in most cases. Overall, the numbers are somewhat below the leading OVO classification results. However, the ILSTSVM manages to excel in two cases.

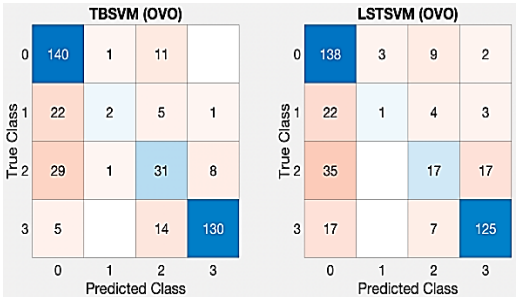

Figure 9. Confusion matrices from using TBSVM (mv+md) and LSTSVM

Parameter Influence On Accuracy

We further investigate how changes of the penalty parameters and the RBF kernel parameter σ change the predictive accuracy rate for some of the machine models.

Figure 10 shows the influence of the penalty parameter C and the kernel parameter σ on the one-versus-one and one-versus-all SVM recognition rates. In both cases, the graphs show that the penalty parameter has more of an influence on accuracy than the kernel parameter. High values of C are required for good accuracy, while the kernel parameter σ remains in a medium range.

In one-versus-one, the accuracy remains constantly low for small C values and then rapidly increases as C becomes larger. However, in one-versus-all the accuracy shows gradual improvement as C goes higher.

For the TWSVM, from Figures 11 and 12 it can be seen that the situation is reversed: relatively low values of the penalty parameters and kernel parameter give good accuracy, and the results are similar for all the different decision strategies. In contrast to the SVM, the accuracy suddenly degrades as the value of C_1=C_2 increases. However, one can notice a slight improvement in

Table 3. Multi-class classification (one-versus-one)

Classifier	Parameters C_1=C_2,C_3=C_4, σ	Accuracy-1	Accuracy-2	Sensitivity	Specificity	Precision
SVM	2^{8}, n/a ,2^{-1}	74.55 ±4.98	87.4 ±0.15	56.39 ±0.47	90.58 ±0.11	63.32 ±1.81
TWSVM (mv)	2^{0}, n/a, 2^{1}	73.57 ±5.37	86.79 ±0.31	54.15 ±0.56	89.96 ±0.21	60.51 ±2.29
TWSVM (md+mv)	$2^{-0.25}$, n/a, 2^{1}	74.73 ±5.45	87.36 ±0.28	56.33 ±0.73	90.55 ±0.22	64.29 ±2.40
TBSVM (mv)	2^{0}, 2^{-16}, 2^{1}	74.05 ±4.84	87.03 ±0.42	55.44 ±1.00	90.29 ±0.30	63.75 ±4.06
TBSVM (md+mv)	2^{0}, 2^{-16}, 2^{1}	75.18 ±5.52	87.59 ±0.31	56.51 ±0.80	90.71 ±0.23	66.37 ±5.48
LSTSVM (mv)	2^{-5}, n/a ,2^{0}	71.35 ±5.48	85.68 ±0.74	50.97 ±1.53	88.98 ±0.54	53.25 ±6.24
LSTSVM (md)	$2^{-4.75}$,n/a, $2^{-0.25}$	73.15 ±5.63	86.58 ±0.41	53.91 ±0.89	89.93 ±0.29	52.56 ±3.01
ILSTSVM (mv)	2^{-5}, 2^{-19}, 2^{1}	73.03 ±4.58	86.51 ±0.46	52.67 ±0.93	89.74 ±0.32	55.98 ±6.07
ILSTSVM (md)	2^{-5}, 2^{-19}, 2^{1}	74.33 ±4.67	87.06 ±0.46	55.13 ±1.02	90.46 ±0.31	56.03 ±8.37

Table 4. Multi-class classification (one-versus-all and all-versus-one)

Classifier	Parameters C_1=C_2, C_3=C_4, σ	Accuracy-1	Accuracy-2	Sensitivity	Specificity	Precision
one-versus-all						
SVM	2^{10}, n/a, $2^{-1.25}$	73.38 ±4.67	86.69 ±0.48	53.83 ±1.03	89.85 ±0.34	60.46 ±4.02
TWSVM	2^{-1}, n/a, 2^{0}	73.57 ±5.07	86.79 ±0.39	54.48 ±1.11	90.03 ±0.30	60.80 ±4.38
TBSVM	2^{-1}, 2^{-13}, 2^{0}	73.88 ±5.03	86.94 ±0.47	55.00 ±0.80	90.16 ±0.31	62.13 ±3.53
LSTSVM	2^{-1}, n/a, 2^{-3}	68.40 ±6.04	84.20 ±0.53	50.71 ±1.09	88.35 ±0.36	51.86 ±1.55
ILSTSVM	2^{-1}, 2^{-2}, 2^{-3}	71.35 ±5.12	85.68 ±0.35	51.20 ±0.69	88.80 ±0.26	67.50 ±0.62
all-versus-one						
TWSVM	2^{1}, n/a, 2^{-1}	70.83 ±4.78	85.41 ±0.33	52.54 ±0.72	89.05 ±0.24	58.50 ±2.67
TBSVM	2^{1}, 2^{-5}, 2^{-2}	72.43 ±5.45	86.21 ±0.44	53.42 ±0.83	89.50 ±0.32	61.32 ±3.28
LSTSVM	2^{-3}, n/a, 2^{-1}	68.43 ±5.23	84.21 ±0.56	47.55 ±1.18	87.77 ±0.49	50.60 ±4.45
ILSTSVM	2^{5}, 2^{-2}, 2^{-4}	71.95 ±6.29	85.98 ±0.36	53.77 ±0.67	89.39 ±0.26	59.83 ±2.01

the accuracy rate when using the minimum average distance to break the tie in votes from maximum-votes strategy (mv+md).

In the case of the LSTSVM, from Figures 13 and 14, one-versus-one and all-versus-one seem to require relatively low values of C_1=C_2 and σ for good accuracy. The surface remains flat for the one-versus-one case, and we notice some improvement in the overall rate of accuracy when using our new method of classifying by minimum average distance as seen in Figure 13(b). For one-versus-all, a higher penalty parameter gives better performance. In all cases, performance is best when the kernel parameter σ is in the neighborhood of 2^0. An exception are the least square twin SVMs, where σ may be as low as 2^{-4} which can be seen from Tables 3 and 4.

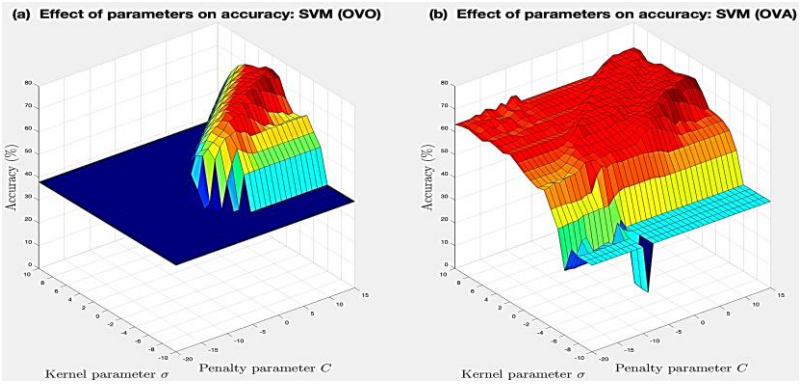

Figure 10. Effect of *C*, σ on accuracy of SVM

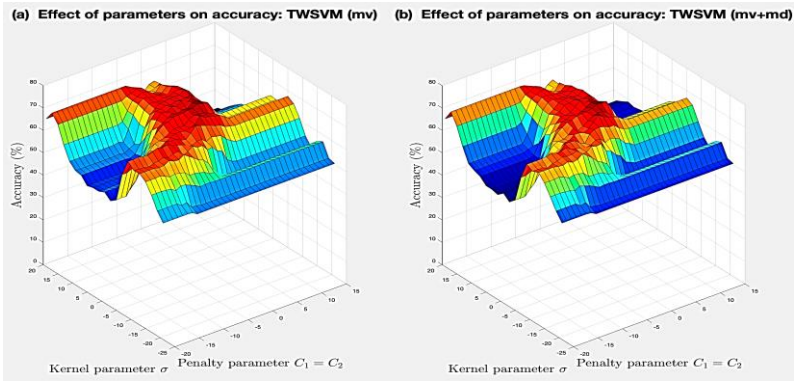

Figure 11. Effect of C_1=C_2, σ on accuracy of TWSVM (OVO)

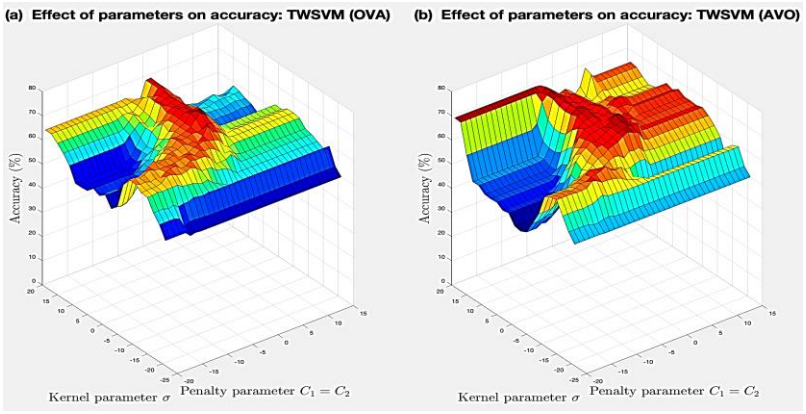

Figure 12. Effect of C_1= C_2, σ on accuracy of TWSVM (OVA and AVO)

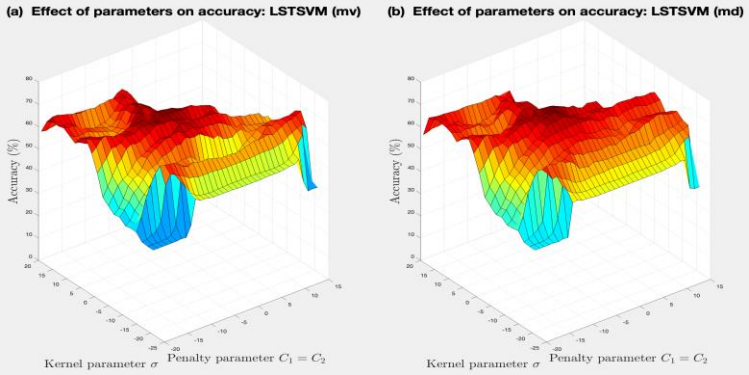

Figure 13. Effect of $C_1 = C_2$, σ on accuracy of LSTSVM (OVO)

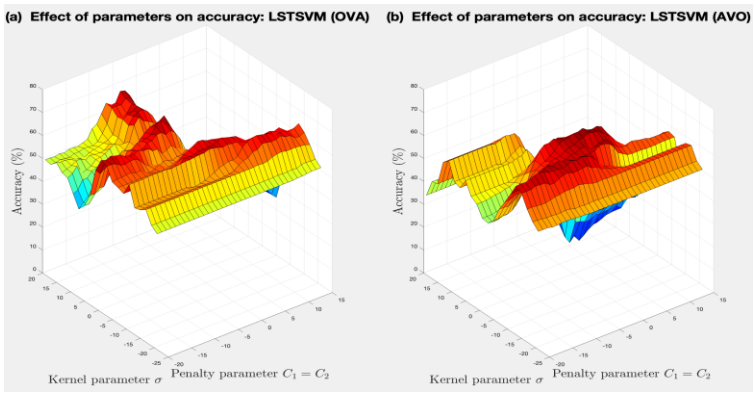

Figure 14. Effect of $C_1 = C_2$, σ on accuracy of LSTSVM (OVA and AVO)

Discussion

In binary classification, all types of SVMs produced good results. Twin-type support vector machine models did not show any advantage over the standard support vector machine but are close behind. In addition, least-squares based models fall somewhat behind the other models. However, the improved least squares twin SVM (ILSTSVM) comes close to the twin SVM (TWSVM) in overall performance and bypasses it in sensitivity.

On the other hand, when optimized for sensitivity instead of accuracy, the least squares twin SVM and the improved least squares twin SVM show the most balanced picture regarding all four-performance metrics used.

In multi-class problems the overall performance is noticeable lower than in binary classification. We should note, however, that in binary classification, the mild and moderate images which are the most difficult ones to classify, are disregarded. The twin bounded support vector machine (TBSVM) showed the best performance in almost all multiclass metrics. However, the standard SVM and twin SVM follow close behind.

The least squares based models showed again lower performance, although the improved least squares SVM managed to catch up in some of the metrics.

The one-versus-one decisions tend to be better than the one-versus-all decisions which in turn tend to be slightly better than the all-versus-one decisions. The difficulties in multi-class decisions are mainly due to the fact that most of the mild and moderate images are not being detected as being in the diseased class. In mild NPDR eye images, the paramount characteristics are the microaneurysms. Their separating out is the most difficult among all the segmentation tasks as it depends more than others on factors such as image quality or the basic or advanced image preprocessing techniques used.

As for the moderate NPDR images, haemorrhages and cotton wool spots can be observed as per clinical pathologies in general. However, the Messidor dataset contains several NPDR images labeled moderate which do not exhibit these properties. In addition, only a few microaneurysms are present in these moderate images, just as in the mild case. Thus, the distinction between these classes seems subtle. It remains a challenge to improve on the image pre-

processing and feature extraction techniques in order to be better able to detect the mild and moderate cases.

Comparison with results in the literature. Carrera *et al*. (2017) have used the Messidor database as well and have performed binary classification using the regular SVM involving normal and severe NPDR graded images as shown in Table 5. They have obtained rates of accuracy and sensitivity, respectively, as 92.4% and 94.6% from 10- fold cross validation. The authors have also reported binary classification results using a decision tree (DT). Whether optimized for accuracy or sensitivity, our results show better numbers.

They have further evaluated and reported performance of multi-class classifications based on a single run of 10- fold cross validation as given in Table 6, and obtained an accuracy-2 of 85.1%, sensitivity of 49.4%, and specificity of 88.4%. Again, our performance numbers are noticeably better. In addition, our results compare favorably to the ones published in (Maher *et al.*, 2015). These superior results are likely due to the careful image preprocessing and feature extraction described above.

Conclusions

In this research, we have presented the classification of eye fundus images with regards to the various stages of nonproliferative diabetic retinopathy using support vector machines.

The procedure began by delineating the various image processing techniques for the detection in eye fundus images of retinal blood vessels, microaneurysms, haemorrhages, exudates, which are the markers for diabetic retinopathy, as well as the optic disk. These four markers were extracted from the algorithms as the most significant features. They were supplemented by another nine features extracted, based on statistical and texture content from the green channel of the image and its gray-level co-occurrence matrix. In total 13 features were extracted to be fed to the classifiers.

Then various support vector machine models were employed, first for detection of severe nonproliferative diabetic retinopathy, and next for detection and multi-class grading of nonproliferative diabetic retinopathy.

For the detection of severe nonproliferative diabetic retinopathy, 7 of the 13 features gave optimal results with an accuracy rate of 97.44±2.91% from the standard support vector machine. When the goal was to optimize for sensitivity, the twin bounded support vector machine yielded the highest sensitivity of 99.06±2.52%.

In case of nonproliferative diabetic retinopathy grading, the best performances were recorded using 11 features. The twin bounded support vector machine with the novel 'maximum-vote and minimum average distance as the tie breaker' strategy recorded highest performance rates with an average accuracy of 87.59% with standard deviation of ±0.31%. The performance metrics other than accuracy were also marginally higher on this machine when compared to the other classifiers.

The two twin least square support vector machines showed the least performance of all classifiers, however, in the one-versus-one decision

Table 5. Binary classifications results comparisons with literature

	Classifier	Accuracy	Sensitivity	Specificity	Precision
Accuracy optimized					
(This work)	SVM	97.44 ±2.91	96.65 ±4.52	98.22 ±3.75	98.30 ±3.48
(Carrera et al.)	SVM	92.4	87.3	97.4	97.2*
(Carrera et al.)	DT	92.0	86.6	97.4	n/a
Sensitivity optimized					
(This work)	SVM	90.17 ± 4.80	98.35 ± 3.35	82.55 ± 8.94	85.10 ± 6.89
(This work)	TBWSVM	91.53 ± 4.77	99.06 ± 2.52	84.18 ± 9.53	86.56 ± 7.16
(This work)	ILSTSVM	94.05 ± 4.19	98.66 ± 3.01	89.53 ± 7.40	90.63 ± 6.20
(Carrera et al.)	SVM	80.4	94.6	66.2	n/a
(Carrera et al.)	DT	91.0	94.0	88.1	n/a

*****: not published in Carrera *et al.* (2017) but computed from the published confusion matrix.

Table 6. Multi-class classification results comparisons with literature (one-versus-one)

	Classifier	Accuracy-1	Accuracy-2	Sensitivity	Specificity	Precision
(This work)	TBSVM (mv+md)	75.18± 5.52	87.59± 0.31	56.51 ±0.80	90.71 ±0.23	66.37 ±5.48
(This work)	SVM	74.55 ±4.98	87.40 0.15	56.39 ±0.47	90.58 ±0.11	63.32 ±1.81
(Carrera et al.)	SVM	70.3*	85.1	49.4	88.4	49.3*

*****: not published in Carrera *et al.* (2017) but computed from the published confusion matrix.

method, their performance was noticeably increased when "minimum average distance from the hyperplane" strategy was applied.

Overall, all models displayed similar performance, differing by not more than a few percentage points. Nevertheless, a careful selection of the support vector machine model and decision strategy can help achieve the optimum.

Our results turned out to be superior to most presented in the literature. This is likely due to the careful image preprocessing and feature selection. However, the detection of mild and moderate diabetic retinopathy still presents a challenge. Many of the images in the Messidor database that are classified as mild or moderate are difficult to distinguish from healthy images even with the naked eye, as they are characterized mainly by microaneurysms. Similarly, the automatic extraction of microaneurysms proved far from perfect, whereas the extraction of blood vessels, exudates and haemorrhages was fairly successful. It would be worthwhile to investigate feature extraction methods using other machine learning methods, such as convolutional neural networks for example, to explore the small specific nuances in the images as new features.

Acknowledgement

J. Namgyal gratefully appreciates the support received from Suranaree University of Technology through a Vithibundit Graduate Scholarship.

References

Acharya, U.R., Chua, C.K., Ng, E.Y.K., Yu, W., and Chee, C. (2008). Application of higher order spectra for the identification of diabetes retinopathy stages. J. Med. Syst., 32(6):481-488. https://doi.org/10.1007/s10916-008-9154-8

Ali, J.,Aldhaifallah, M., Nisar, K.S., Aljabr, A.A. and Tanveer, M. (2021). Regularized least squares twin SVM for multiclass classification. Big Data Res., 27:100295. https://doi.org/10.1016/j.bdr.2021.100295

American Academy of Ophthalmology. (2019). Fundamentals and Principles of Ophthalmology. Basic and Clinical Science Course, 546p.

Bhardwaj, C., Jain, S. and Sood, M. (2020). Hierarchical severity grade classification of non-proliferative diabetic retinopathy. J. Ambient. Intell. Humaniz. Comput., 12:2,649-2,670. https://doi.org/10.1007/s12652-020-02426-9

Carrera, E.V., González, A. and Carrera, R. (2017). Automated detection of diabetic retinopathy using SVM, The 2017 IEEE XXIV International Conference on Electronics, Electrical Engineering and Computing (INTERCON), p. 1-4. https://doi.org/10.1109/INTERCON.2017.8079692

Chang, C.C., and Lin, C.J. (2011). LIBSVM: A library for support vector machines. ACM Trans. Intell. Syst. Technol., 2(3):1-27. https://doi.org/10.1145/1961189.1961199

Chen, B., Wang, L., Wang, X., Sun, J., Huang, Y., Feng, D. and Xu, Z. (2020). Abnormality detection in retinal image by individualized background learning. Pattern Recognit., 102:107209. https://doi.org/10.1016/j.patcog.2020.107209

Dandapat, S., Ghosh, S., Si, S. and Datta, A. (2021). Analysis of diabetic retinopathy abnormalities detection techniques. Proceedings of International Conference on Frontiers in Computing and Systems. Advances in Intelligent Systems and Computing, vol 1255. Springer, Singapore, p. 235-247. https://doi.org/10.1007/978-981-15-7834-2_22

Decencière, E., Zhang, X., Gazuguel, G., Lay, B., Cochener, B., Trone, C., Gain, P., Ordonez, R., Massin, P., Erginay, A., Charton, B., and Klein, J.C. (2014). Feedback on a publicly distributed database: the Messidor database. Image Analysis & Stereology, 33(3):231-234. https://doi.org/10.5566/ias.1155

Ghosh, R., Ghosh, K., and Maitra, S. (2017). Automatic detection and classification of retinopathy stages using CNN, Proceedings of the 4th International Conference on Signal Processing and Integrated Networks (SPIN 2017), p. 550-554. https://doi.org/10.1109/SPIN.2017.8050011

Gonzalez, R.C., Woods, R.E., and Eddins, S.L. (2009). Digital Image Processing Using MATLAB. 2nd. ed. Gatesmark Publishing, United States, 827p.

Hemanth, J., Deperlioglu, O., and Kose, U. (2020). An enhanced diabetic retinopathy detection and classification approach using deep convolutional neural network. Neural Comput & Applic., 32:707-721. https://doi.org/10.1007/s00521-018-03974-0

Imani, E., Pourezza, H.R. and Banaee, T. (2015). Fully automated diabetic retinopathy screening using morphological component analysis. Computerized Medical Imaging and Graphics, 43:78-88. https://doi.org/10.1016/j.compmedimag.2015.03.004

James, J., Sharifahmadian, E., and Shih, L. (2018). Automatic severity level classification of diabetic retinopathy. International J. Comput. Appl., 180(12):30-35. https://doi.org/10.5120/ijca2018916244

Kandhasamy, J.P., Balamurali, S., Kadry, S., and Ramasamy, L.K. (2020). Diagnosis of diabetic retinopathy using multi level set segmentation algorithm with feature extraction using SVM with selective features. Multimed. Tools. Appl., 79:10,581-10,596.

Katada, Y., Ozawa, N., Masayoshi, K., Ofuji, Y., Tsubota, K., and Kurihara, T. (2020). Automatic screening for diabetic retinopathy in interracial fundus images using artificial intelligence. Intelligence-Based Medicine, 3-4:100024. https://doi.org/10.1016/j.ibmed.2020.100024

Li, Y.H., Yeh, N.N., Chen, S.J., and Chung, Y.C. (2019). Computer-assisted diagnosis for diabetic retinopathy based on fundus images using deep convolutional network. Mob. Inf. Syst., 2019:6143839. https://doi.org/10.1155/2019/6142839

Maher, R., Kayte, S., and Dhopeshwarkar, D.M. (2015). Review of automated detection for diabetes retinopathy using fundus images. Int. J. Adv. Res. Comput. Sci. Eng. Inf. Technol., 5(3):1,129-1,136.

Namgyal, J., and Schulz, E. (2022). A Novel Decision Method for Multiclass Twin Support Vector Machines by Average Distance. The First Annual meeting in Mathematics (AMM2022), p. 57-76.

Ramos-Soto, O., Rodríguez-Esparza, E., Balderas-Matta, S.E., Oliva, D., Hassanien, A.E., Meleppat, R.K., and Zawadzki R.J. (2021). An efficient retinal blood vessel segmentation in eye fundus images by using optimized top-hat and homomorphic filtering. Computer Methods and Programs in Biomedicine, 201:105949. https://doi.org/10.1016/j.cmpb.2021.105949

Sarki, R., Ahmed, K., Wang, H. and Zhang, Y. (2020). Automatic detection of diabetic eye disease through deep learning

using fundus images: a survey. IEEE Access, 8: 151133-151148. https://doi.org/10.1109/ACCESS.2020.3015258

Welikala, R.A., Fraz, M.M., Dehmeshki, J., Hoppe, A., Tah, V., Mann, S., Williamson, T.H., and Barman, S.A. (2015). Genetic algorithm-based feature selection combined with dual classification for the automatic detection of proliferative diabetic retinopathy. Computerized Medical Imaging and Graphics, 43:64-77. https://doi.org/10.1016/j.compmedimag.2015.03.003

World Health Organization. (2015). TADDS: Tool for the Assessment of Diabetic Retinopathy and Diabetes Management Systems. Available from: https://apps.who.int/iris/rest/bitstreams/1242602/retrieve